THE JOURNAL OF PHYSICAL CHEMISTRY B
A JOURNAL OF THE AMERICAN CHEMICAL SOCIETY

pubs.acs.org/JPCB Article

Shell-Isolated Assembly of Atomically Precise Nanoclusters on Gold Nanorods for Integrated Plasmonic-Luminescent Nanocomposites

Published as part of The Journal of Physical Chemistry virtual special issue "Kankan Bhattacharyya Festschrift".

Amrita Chakraborty, Harsh Dave, Biswajit Mondal, Nonappa, Esma Khatun, and Thalappil Pradeep*

Cite This: *J. Phys. Chem. B* 2022, 126, 1842−1851 Read Online

ACCESS | Metrics & More | Article Recommendations | SI Supporting Information

ABSTRACT: In this work, we integrate atomically precise noble metal nanoclusters (NCs) on gold nanorods (AuNRs) to create hybrid plasmonic-luminescent nanomaterials. Initially, we assemble luminescent $Ag_{29}(LA)_{12}$ NC (LA = lipoic acid) to silica shell-encapsulated AuNRs. The resulting nanostructure shows plasmon-enhanced luminescence in aqueous medium as well as in the solid state. Atomic precision of the fluorophores used in this case allows detailed characterization of individual nanocomposites by diverse techniques, including transmission electron microscopy (TEM) and 3D electron tomographic reconstruction. We extend this strategy to prepare similar structures with gold NC protected with bovine serum albumin (Au_{30}BSA). These two examples demonstrate the generic nature of the present strategy in preparing plasmonic-luminescent hybrid nanostructures using atomically precise NCs.

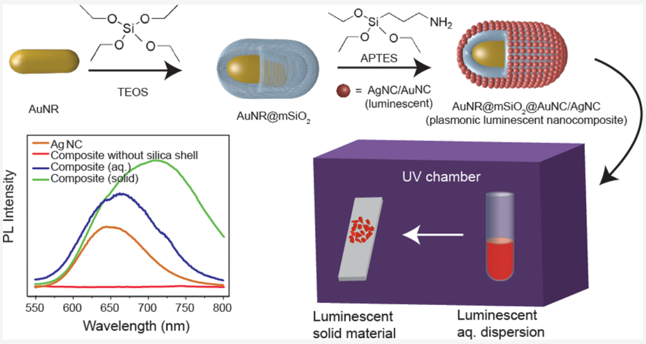

■ INTRODUCTION

The size- and shape-dependent optoelectronic, mechanical, and chemical properties of nanoscale materials make them important in numerous fields such as water purification,[1] renewable energy,[2] catalysis,[3] sensing,[4] and therapy.[5] Metallic nanoparticles (NPs) of <2 nm diameter are termed as nanoclusters (NCs). They are atomically precise and therefore have molecule-like absorption features. NCs show unusual optoelectronic properties compared to larger plasmonic NPs. For example, some of them exhibit bright luminescence, which has found applications in bioimaging, biolabeling, and diagnostics.[6,7] Among the imaging-based diagnosis techniques, fluorescence imaging is immensely popular for early cancer detection due to its low cost, high sensitivity, and high spatial resolution. However, conventional dyes like rhodamine 6G show ultrabright fluorescence and a quantum yield (QY) as high as 80%, but they undergo photobleaching.[8] Also, molecular dyes are cytotoxic; they often drip out of the cytoplasm during fluorescence microscopy in the case of live-cell imaging. Bright photoluminescence, high quantum yield, significant photostability, and large Stokes shifts are typical of a good contrast agent. Semiconductor QDs like CdSe, CdTe, CdS, ZnS, ZnSe, PbS, and PbSe show high luminescence intensity and quantum yield, significant stability against photobleaching, and narrow and symmetric emission spectra that are tunable over a broad range of wavelengths from UV to NIR region.[9] However, with a few exceptions like silicon QDs[10] and carbon dots,[11] most of the QDs cause cytotoxicity due to the presence of heavy metal ions and tend to aggregate inside the cell, which prevents their extensive use in therapeutic applications.[12] On the contrary, a number of luminescent noble metal NCs display relatively low cytotoxicity and high biocompatibility. In the case of protein-protected NCs, complex 3D structures of proteins can withstand a wide range of pH.[13] Besides, their ultrafine sizes help the cells to retain their regular biophysical functions in their unaltered state.[14] Size uniformity and good mechanical strength of atomically precise NCs make them better candidates as multifunctional fluorophores compared to most semiconductor QDs, owing to the difficulty in precise size control. Therefore, efforts are being made to improve the luminescence and photostability of NCs in the recent past.[15,16] A straightforward approach in this direction is to conjugate luminescent Au and Ag NCs to plasmonic NPs, as they enhance the local electric field in the surroundings. Any fluorophore is greatly affected by the surface plasmon of the NPs in close proximity.[17] However, depending on the distance between them, this interaction is known to either enhance (by

Received: December 1, 2021
Revised: January 30, 2022
Published: February 18, 2022

https://doi.org/10.1021/acs.jpcb.1c10207
J. Phys. Chem. B 2022, 126, 1842−1851

far-field energy transfer) or quench (due to nonradiative decay) the photoluminescence (PL) intensity of the fluorophore. As a result, assembling dye molecules or QDs with a central plasmonic NP, surrounded by a nonmetallic oxide or polymer shell, has been tried.[18] Use of noble metal NCs in this context is promising, yet limited. Plasmonic noble metal NPs of nonspherical shape exhibit shape-dependent physicochemical properties. For example, gold nanorods (AuNRs) exhibit strong absorption and scattering in the near-infrared (NIR) region, where most human tissues, intrinsic chromophores, hemoglobin, and water show very poor absorbance, making it an efficient nanoprobe for *in vivo* biomedical imaging, drug delivery, and phototherapy.[19] Since a combination of multiple imaging modalities offers synergistic advantages over single techniques, recent emphasis has been to develop hybrid nanomaterials where different NPs of various properties are integrated into a single nanostructure. These structures exhibit combined qualities of their components leading to efficient multimodal nanoprobes.[20−23] Importantly, mesoporous silica-coated AuNRs, when loaded with indocyanine green, act as a contrast agent for computed tomography (CT) scan and fluorescence dual mode imaging.[24] Conjugation of Gd(III) ions with AuNRs has resulted in a single nanoprobe for simultaneous magnetic resonance imaging (MRI) and CT imaging.[25] Anisotropic NPs are also attractive as building blocks of plasmonically engineered metamaterials as they induce directional interaction.[26] Recent studies have shown that NCs can take part in the colloidal assembly within themselves,[27] as well as with 1D plasmonic NPs, producing precision assemblies.[28,29] Therefore, it is interesting to create a binary assembly of anisotropic noble metal NPs and luminescent NCs and investigate the effect of surface plasmons on the photophysical properties of the NCs.

Herein, we introduce a multimodal imaging probe by loading luminescent noble metal NCs onto AuNRs protected by a silica shell of uniform thickness, and study the structures and photophysical properties of the composite nanostructures. Lipoic acid (LA)-protected Ag NC, $Ag_{29}(LA)_{12}$ (abbreviated as Ag_{29}), is chosen as the luminescent component, which is ultrasmall in size, atomically precise, and distinctly visible using transmission electron microscopy. This is conjugated to AuNRs through a mesoporous silica shell, leading to a nanocomposite where the luminescence of Ag_{29} is enhanced due to plasmonic coupling. Using 3D tomographic reconstruction of the transmission electron micrographs, we study the growth of silica shells on AuNR surface facets and the attachment of Ag_{29} NCs to the mesoporous shell. We have also conjugated Au_{30}BSA (BSA= bovine serum albumin), one of the extensively studied luminescent NCs for live-cell imaging with silica-coated AuNR, in a similar approach. In both cases, the PL intensity of the NC was enhanced due to plasmonic coupling, demonstrating the generic nature of the strategy. We believe that the precise structural insights presented will encourage the community to explore NCs with diverse functionality and rich surface chemistry to design composite nanomaterials that may be useful for applications beyond multimodal bioimaging, such as targeted drug delivery and biosensing.

■ EXPERIMENTAL METHODS

Chemicals. Gold(III) chloride trihydrate ($HAuCl_4 \cdot 3H_2O$), cetyltrimethylammonium bromide (CTAB), sodium borohydride ($NaBH_4$), tetraethyl orthosilicate (TEOS), and (3-aminopropyl) triethoxysilane (APTES) were purchased from Sigma-Aldrich, USA. Lipoic acid (LA), silver nitrate ($AgNO_3$), ascorbic acid, and sodium hydroxide (NaOH) were purchased from Rankem India Pvt., Ltd. BSA was purchased from HiMedia Pvt., Ltd. Deionized (DI) water was used for all syntheses.

Methods. *Synthesis of AuNRs.* The synthesis of AuNRs was carried out using the protocol proposed by Samal et al.[30] In this wet chemical synthesis method, 20 mL of 100 mM CTAB was added to a conical flask to which, sequentially, 1 mL of 10 mM $HAuCl_4 \cdot 3H_2O$, 130 μL of 10 mM $AgNO_3$, and 140 μL of 100 mM ascorbic acid were added with mild stirring. Then, 200 μL of a freshly prepared ice-cold $NaBH_4$ solution (1.67 mM) was quickly injected into the reaction mixture and stirring was stopped immediately. Although the dark brown color, characteristic of AuNRs, appeared within 0.5 h, this growth medium was kept still for at least 4 h to ensure a high yield of the AuNRs. The temperature was maintained at 28 °C throughout the synthesis. Finally, the mixture was centrifuged twice at 13 000 rpm for 12 min. Each time the supernatant was discarded by decanting, and the pellet was redispersed in DI water.

Synthesis of AuNR@mSiO_2 (Where m= Thickness of Silica Shell). To grow a mesoporous silica shell encapsulating the AuNRs, we followed the previously reported method.[31] However, for different shell thicknesses, the protocol was slightly modified to achieve the best result.

Silica Shell of 8 ± 0.76 nm Thickness, Denoted as AuNR@8SiO_2. First, 10 mL of purity AuNRs (optical density, i.e., O.D. = 1.2 at 780 nm) was taken in a 30 mL glass vial. The pH was adjusted to 10−10.4 by slowly adding 100 μL of 100 mM NaOH upon continuous stirring until the pH was stable. To the reaction mixture, 90 μL of 20% TEOS (v/v in methanol) was added in three portions of 30 μL each with 30 min interval between each addition. The reaction was continued for 24 h, and then the product was precipitated by centrifugation at 11 000 rpm for 12 min. DI water was used to remove excess silica.

Silica Shell of 12 ± 0.95 nm Thickness, Denoted as AuNR@12SiO_2. The synthesis was performed as described for AuNR@8SiO_2. In brief, 8 mL of the AuNR batch (OD = 1.2 at 780 nm) was used and the pH was adjusted to 10−10.4. 15 μL of 20% TEOs was added in 3 steps and the reaction was continued for 12 h. The product was precipitated using centrifugation and purified by washing with DI water, as described before.

Silica Shell of 16 ± 0.84 nm Thickness, Denoted as AuNR@16SiO_2. This was a two-step process. The first step was similar to that of AuNR@12SiO_2. After the unbound silica was removed from the product by decanting the supernatant, the pellet of AuNR@12SiO_2 was dispersed in 8 mL of DI water. By adding 100 mM NaOH under stirring conditions, we adjusted the pH of the solution and the same protocol was repeated. Finally, the product was washed in a similar fashion by centrifugation at 11 000 rpm for 12 min.

Amine-Functionalization of AuNR@mSiO_2. The silica shell was modified by adding an end-functional group according to a previous report with some customization.[32] Briefly, 12.5 μL of APTES was added to 10 mL of clean AuNR@mSiO_2 of any silica shell thickness (O.D. 1.2 at 780 nm) under vigorous stirring. Stirring was continued for 2−3 h at room temperature, and the synthesized product was centrifuged at 11 000 rpm for 10 min. The supernatant containing unreacted APTES was

Scheme 1. Schematic of the Growth of Mesoporous Silica Shell on AuNR and Subsequent Addition of $-NH_2$ Functional Group to Finally Attach Luminescent NC

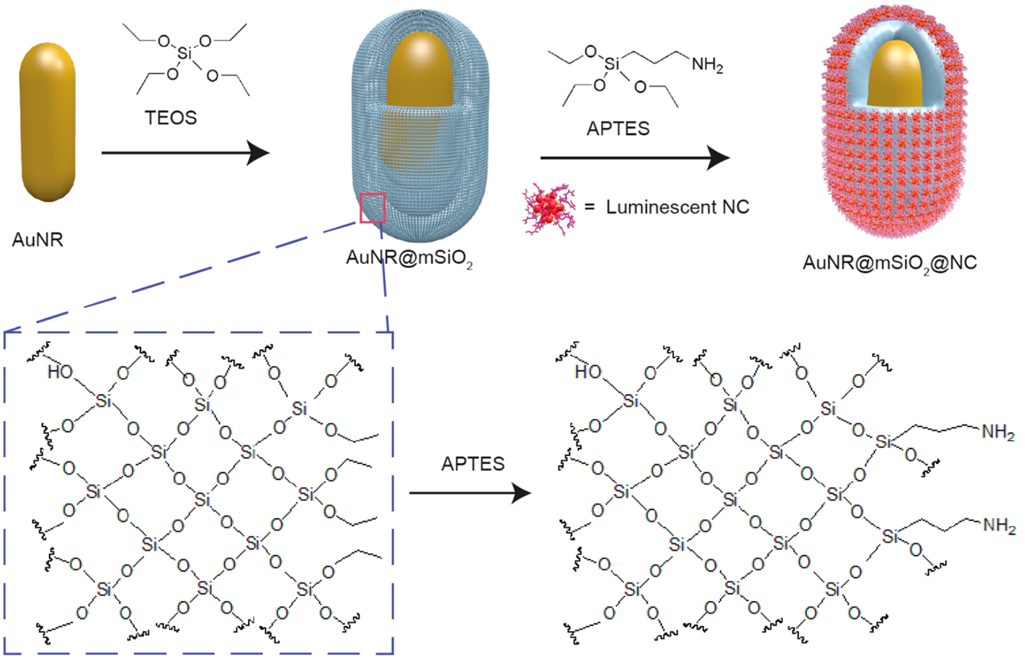

decanted and the precipitate, named AuNR@mSiO$_2$−NH$_2$, was dispersed in DI water.

Synthesis of $Ag_{29}(LA)_{12}$ NCs. The LA-protected Ag NC was synthesized using a previous report.[33] Precisely, 19 mg of LA (92 μmol) and 7 mg of NaBH$_4$ (0.19 mmol) were added to a 30 mL glass vial containing 14 mL of water. The reaction mixture was stirred until all LA had dissolved, and then 700 μL of 25 mM AgNO$_3$ (17.5 μmol) was added, which turned the solution turbid. This was followed by the addition of 10 mg of NaBH$_4$ (0.26 mmol) dissolved in 2 mL of water. The cluster took 3−5 h to form. The reaction vial was wrapped in an aluminum foil to avoid the exposure of the clusters to light. The synthesis was carried out at room temperature. Samples were stored in the dark at 4 °C.

Synthesis of Au_{30}BSA NCs. BSA-protected gold NCs were synthesized as reported previously by Mohanty et al.,[34] where the cluster was assigned as Au$_{30}$BSA based on the MALDI MS. For this, 125 mg of BSA was added to 5 mL of DI water, and the mixture was sonicated until it was fully dissolved. Then, 5 mL of 6 mM HAuCl$_4$ solution was added under mild stirring. After 1 min, 500 μL of freshly prepared 1 M NaOH solution was added. The reaction was allowed to be stirred for 12 h.

Synthesis of AuNR@mSiO$_2$@Ag$_{29}$. According to Beer−Lamberts Law, for a dilute colloidal solution

$$A = \varepsilon \cdot c \cdot l$$

where A = absorbance, ε = molar extinction coefficient, c = concentration, and l = path length. For a given nanosystem (AuNRs or the NCs), since ε and l are constants, $A \propto c$.

We have maintained the concentration of AuNRs and Ag$_{29}$ by keeping their O.D. value fixed throughout. Precisely, 1.5 μL of as-synthesized Ag$_{29}$ NC (O.D. = 2.8 at 328 nm) was taken in a 5 mL glass vial which was kept in dark. To this, 500 μL of freshly synthesized AuNR@mSiO$_2$−NH$_2$ (O.D. = 1 at 780 nm) was added dropwise under moderate stirring (300 rpm). The stirring was stopped after 30 min. The solution was centrifuged at 8000 rpm for 10 min and the supernatant containing unbound NCs was discarded. The precipitate containing AuNR@mSiO$_2$@Ag$_{29}$ was dispersed in 1 mL of DI water and was kept in dark throughout.

Synthesis of AuNR@mSiO$_2$@Au$_{30}$BSA. The procedure was same as that described in the case of Ag$_{29}$. Here, the concentration of Au$_{30}$BSA was maintained such that O.D. = 3 at 365 nm.

UV−Vis Spectroscopy. Optical absorption spectra of the samples were recorded using a PerkinElmer Lambda 25 UV−visible spectrometer. We used Milli-Q water for the baseline sample as well as for diluting the samples. A quartz cuvette of 1 cm path length has been used for all the measurements.

PL Spectroscopy. The PL spectra were measured on a HORIBA JOBIN YVON Nano Log instrument. The slit of the bandpass filters for excitation and emission was set at 3 nm.

High-Resolution Transmission Electron Microscopy. A 3 μL aliquot of each sample was drop-cast on a TEM grid (made of copper, 300 mesh) and allowed to dry under ambient conditions. The images were then collected using a JEOL 3010 transmission electron microscope with an accelerating voltage of 200 kV.

Serial EM and Electron Tomography Reconstruction. Copper grids (300 mesh) with an ultrathin carbon support film were used to prepare specimen for electron tomography reconstruction. The specimen preparation was carried out by adding 3 μL of the sample on a plasma-cleaned TEM grid and allowed to dry under ambient conditions. The images acquisition was carried out using a JEOL JEM-3200FSC field-emission TEM operated at 300 kV with an Omega-type zero-loss filter. The tilt series of 2D projections (between ±69° angles with 2° increment steps) were recorded using SerialEM software.[35−37] The relignment and final alignment were carried out using IMOD software.[38] Finally, the maximum entropy method (MEM) was used with a custom-made program for reconstruction and colored tomograms were prepared using Chimera software.[37]

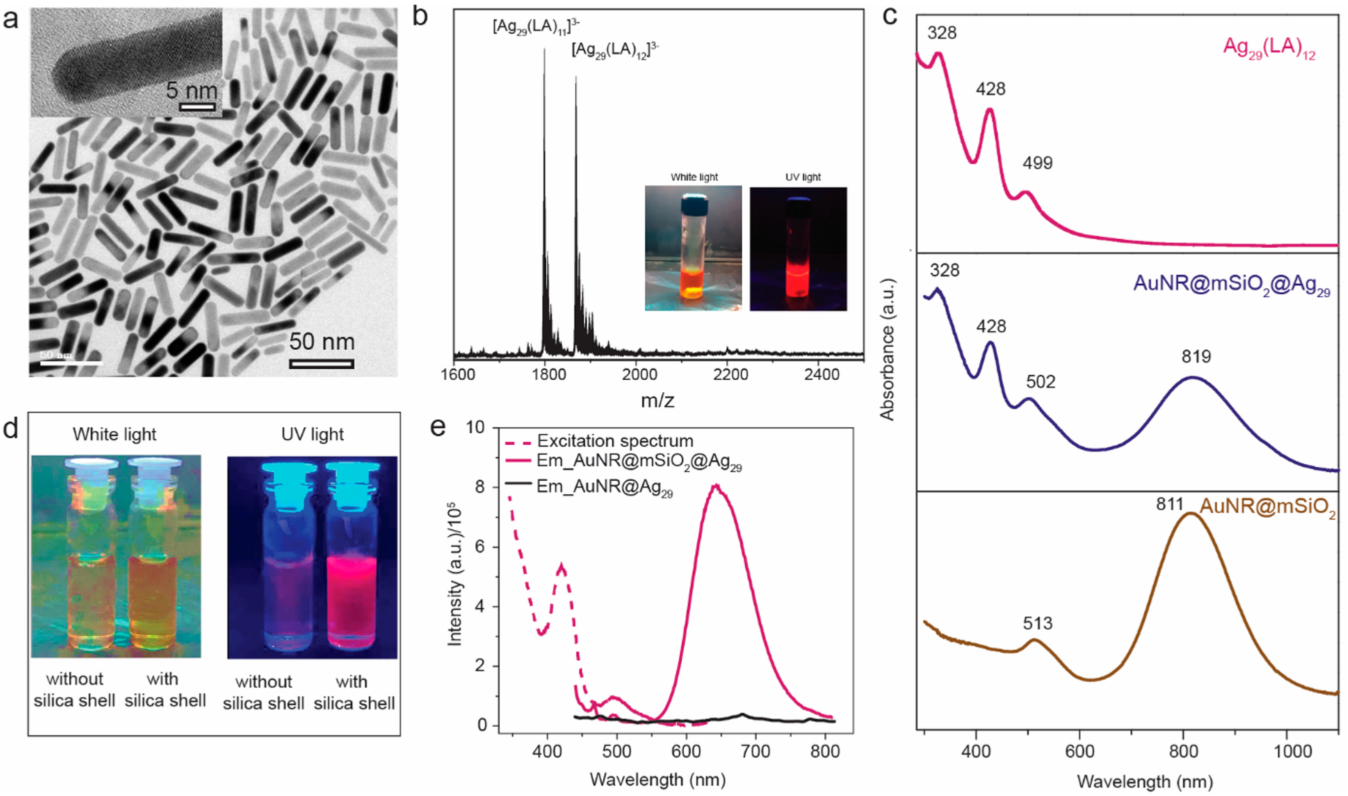

Figure 1. (a) TEM image of AuNRs (HRTEM image of a single AuNR in the inset shows surface facets). (b) ESI MS of Ag_{29} showing a molecular ion peak at $m/z \sim 1868$ along with a peak corresponding to $[Ag_{29}(LA)_{11}]^{-3}$, formed as a byproduct; the inset showing photographs of bright red luminescent Ag_{29} under UV light. (c) Absorption spectra of Ag_{29}, $AuNR@mSiO_2$, and $AuNR@mSiO_2@Ag_{29}$ along with peak positions for comparison. (d) Photograph of $AuNR@Ag_{29}$ (left) and $AuNR@mSiO_2@Ag_{29}$ (right) solutions under white light and UV light. (e) Excitation and emission spectra of $AuNR@mSiO_2@Ag_{29}$ along with the emission spectra of $AuNR@Ag_{29}$ (excitation wavelength= 425 nm for both).

■ RESULTS AND DISCUSSION

Synthesis Strategy and Properties of the Composite Material. Previous studies have shown that direct attachment of fluorophores to a plasmonic core often quenches the PL of the latter, due to near-field damping.[39,40] To retain the PL, lipids, polymers, or amorphous silica shells have been grown on the intrinsic AuNRs. These give enhanced chemical and physical stability to the AuNRs in cellular environment and upon laser exposure and act as spacers between the plasmonic NP and the fluorophores, preventing PL quenching.[41] Owing to their inexpensive nature, biocompatibility, easy functionalization on the AuNR surface, and further conjugation with a range of fluorophores, we grew amorphous silica encapsulating the AuNRs prior to assembling luminescent NCs, as shown in Scheme 1. Many seedless and seed-mediated methods are known for synthesizing AuNRs of various aspect ratios with high size and shape uniformity. In this work, we synthesized ultrasmall AuNRs following a simple one-pot synthetic procedure using CTAB as described in the Experimental Section.[30] TEM image of the particles in Figure 1a shows their size and shape uniformity, while the HRTEM in the inset shows the faceted structure of each AuNR.

For growing a silica shell on AuNR, a well-established method developed by Gorelikov et al. was followed with slight modifications, as described in the “Experimental Methods” section.[31] The resulting composite is abbreviated here as $AuNR@mSiO_2$. The growth of silica shell was initially confirmed from the red shift of the LSPR of parent AuNRs and a change in its zeta potential from +30.4 ± 3 eV to −31 ± 3.5 eV (Figure S1). Subsequently, as depicted in Scheme 1, the $AuNR@mSiO_2$ was treated with APTES that introduced an amine functional group to the silica shell, and the entity is denoted as $AuNR@mSiO_2{-}NH_2$. This step is typically followed to make it interact with the desired fluorophore.[42,43] As the fluorescent component, we chose NCs that show steady and bright PL. LA is a small dithiol that has been used to prepare both Au and Ag NCs.[33,44−46] LA and LA-protected NCs are water-soluble, and their carboxylate ends offer the desired functionality. Therefore, we synthesized LA-protected Ag_{29} NC, namely $Ag_{29}(LA)_{12}$ (abbreviated as Ag_{29}) based on the procedure reported by Linden et al.[33] Formation of Ag_{29} was confirmed from its bright red luminescence, characteristic UV−vis absorption spectrum, and ESI MS spectrum (Figure 1b,c). Freshly prepared $AuNR@mSiO_2{-}NH_2$ was immediately added to Ag_{29} NC under mild stirring condition. After 3−4 h of mixing at room temperature, the material was purified by centrifugation to remove unbound NCs, if any were present. The resulting NC conjugated nanocomposite, denoted as $AuNR@mSiO_2@Ag_{29}$, was thoroughly characterized.

The absorption spectrum of Ag_{29} typically shows sharp bands with maxima around 328, 428, and 499 nm.[33] In contrast, $AuNR@mSiO_2$ exhibits two plasmonic bands: longitudinal surface plasmon resonance (LSPR) at 811 nm and transverse surface plasmon resonance (TSPR) band around 513 nm. Figure 1c shows the comparative absorption spectra of as-synthesized AuNRs, Ag_{29}, and $AuNR@mSiO_2@Ag_{29}$, which reveal that the signature electronic transition bands of Ag_{29} and plasmonic transition band of AuNR were

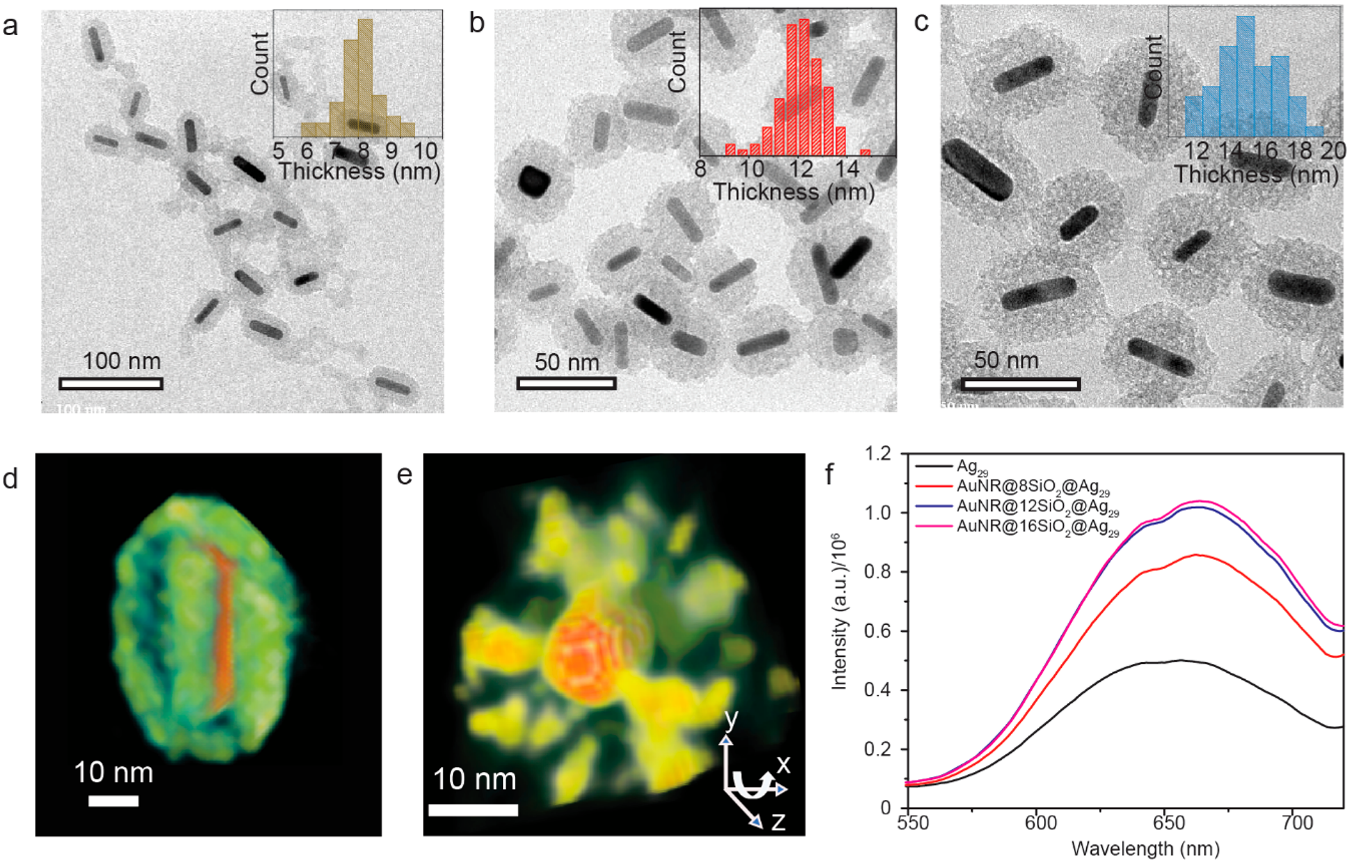

Figure 2. TEM images of AuNR@mSiO_2 with (a) 8 ± 0.76 nm, (b) 12 ± 0.95 nm, and (c) 16 ± 0.84 nm thick silica shells, respectively, along with the distribution of shell thickness in insets. 3D reconstructed TEM tomograms of the (d) side view and (e) top view of AuNR@12SiO_2, (f) comparative emission spectra of AuNR@mSiO_2@Ag_{29} at different shell thickness and that of blank Ag_{29} (all excited at 425 nm).

retained in the resulting composite. As presented in Figure 1d, AuNR@mSiO_2@Ag_{29} showed bright red luminescence under UV light. On the contrary, when we functionalized AuNRs directly by APTES (i.e., without growing any silica shell on them) and made them interact with Ag_{29} in a fashion similar to that used for the control (abbreviated as AuNR@Ag_{29}), no such red luminescence was observed. The PL excitation spectrum of AuNR@mSiO_2@Ag_{29} showed a maximum at 425 nm. When excited at this wavelength, it showed intense PL emission with a maximum at ~650 nm, as depicted in Figure 1e. However, the emission spectrum of AuNR@Ag_{29} showed near-zero intensity throughout the range of visible wavelength. The TEM image of AuNR@Ag_{29} is shown in Figure S2 and suggests that NCs were directly conjugated to AuNRs.

Effect of Silica Shell Thickness. In the case of plasmon-enhanced fluorescence, depending on its distance from the plasmonic NP, luminescence intensity of a fluorophore (both molecular dyes as well as QDs) can either be enhanced or quenched.[47,48] Precisely, the shell thickness plays a crucial role in determining the overall luminescence of the composite in the case of shell-isolated plasmonic-luminescent composites.[41] Here, AuNRs with three different silica shell thicknesses were obtained by optimizing the synthetic protocol (see the “Experimental Methods” section). TEM images along with statistical analyses of silica shell thicknesses are shown in Figure 2a−c, which revealed highly uniform silica shells of thickness 8 ± 0.76 nm, 12 ± 0.95 nm, and 16 ± 0.84 nm, respectively. Although silica coating around AuNR and other NPs has been studied before, their characterization was mostly limited to TEM imaging and optical absorption spectroscopy. However, conventional TEM images show the 2D projection of a 3D object, providing limited information about its true morphology. Hence, we reconstructed the 3D images of individual AuNR@mSiO_2 using a series of 2D projections (Video S1). Figure 2d shows 3D views of a single AuNR@mSiO_2 particle from the side, while Figure 2e shows the view from the tip of the AuNR (90° rotation along the *x*-axis). Unlike in their TEM images, the 3D tomographs of AuNR@mSiO_2 clearly show that the silica shell was not uniformly distributed on the AuNR surface, rather the surface facets of AuNRs were protected alternately. This was true for each AuNR@mSiO_2 particle, irrespective of the thickness of the silica shell. This periodic growth of silica can be explained in terms of differential surface energy of different sets of planes that AuNRs are made of. In our previous studies, 3D images of a single CTAB-coated AuNRs, synthesized in a similar method, revealed its octagonal morphology.[28] According to the literature, these eight planes of AuNRs are made of four (110) and four (100) surface facets arranged alternately.[49] Due to differential surface energies of these facets, metallic Pd,[50] Ag,[51] and Ag NC[28] are known to be deposited preferentially on one of these facets. This finding is important as the plasmonic NPs of different morphologies (e.g., sphere, triangle, cubes, etc.) are made of different sets of surface facets, depending on the synthesis protocol.[52] Thus, the distribution of silica shell encapsulating these structures is likely to differ from one another, which might have a profound effect on their photophysical properties. Here, when the three batches of

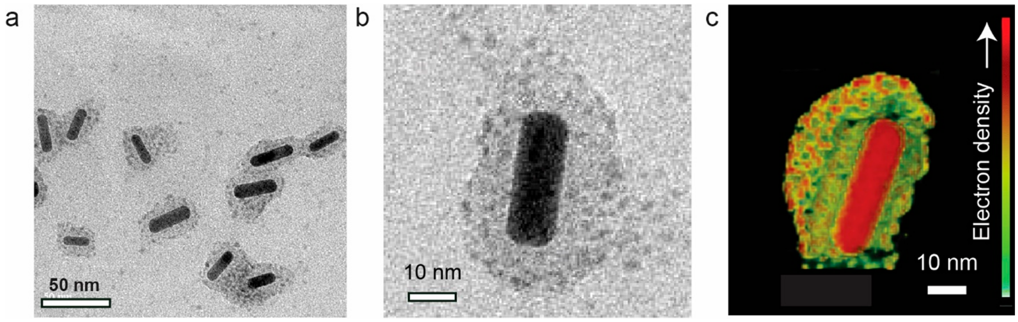

Figure 3. TEM images of (a) AuNR@mSiO$_2$@Ag$_{29}$, (b) single AuNR@mSiO$_2$@Ag$_{29}$, and (c) 3D reconstructed image of (b), where some of the atoms from the front part are omitted to give a clear core−shell view.

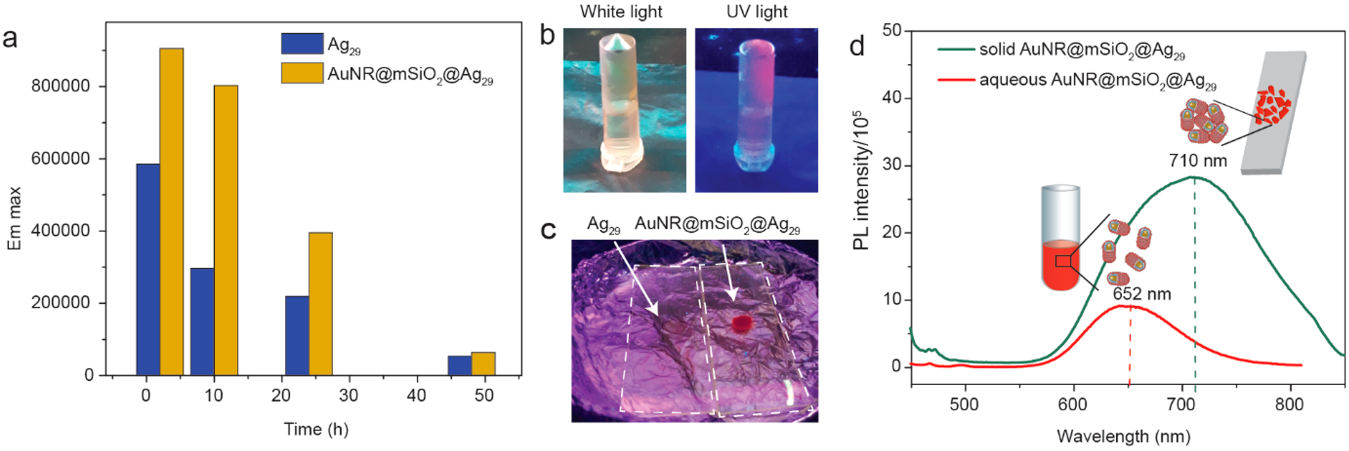

Figure 4. (a) Emission maxima of AuNR@mSiO$_2$@Ag$_{29}$ and blank Ag$_{29}$ plotted against time. (b) Photograph of luminescent AuNR@mSiO$_2$@Ag$_{29}$ spun down from the aqueous dispersion. (c) Photograph under UV light showing comparative luminescence of solid AuNR@mSiO$_2$@Ag$_{29}$ and solid Ag$_{29}$ (the glass slides are marked by white dashed lines for clear visibility). (d) Comparative PL spectra of AuNR@mSiO$_2$@Ag$_{29}$ in aqueous solution and solid phases; schematic showing the aggregation causing the red shift of the spectrum.

AuNR@mSiO$_2$ were functionalized with APTES and subsequently treated with Ag$_{29}$ under the same conditions, AuNR@8SiO$_2$@Ag$_{29}$ showed enhanced luminescence compared to the blank cluster (Figure 2f). In the case of AuNR@12SiO$_2$@Ag$_{29}$, the enhancement was even greater, but upon going to 16 nm thick silica shell, we found no significant change in the PL intensity. Therefore, we carried out all the subsequent experiments with AuNR@12SiO$_2$@Ag$_{29}$.

Structural Insight into the Nanocomposite. Silica NPs and silica-coated metallic NPs conjugated with fluorophores such as QDs and organic dyes have proved their utility in diverse ways.[24,53] However, these studies were focused on the performance of the material as a nanoprobe in respective fields, rather than their detailed characterization. Besides, most of these often lead to aggregated nanocomposites with poor colloidal stability, making it difficult to study their structural details. The strictly monodisperse size and shape of NCs make them much more favorable for colloidal assembly compared to QDs, which usually suffer from significant polydispersity. However, due to their metallic core, most NCs can be imaged under high-resolution transmission electron microscopy (HRTEM), unlike the molecular dyes. Here, AuNR@mSiO$_2$@Ag$_{29}$ was thoroughly characterized using TEM and corresponding 3D images.

Figure 3a includes TEM image of AuNR@mSiO$_2$@Ag$_{29}$, which reveals their structural uniformity. An image of a single nanocomposite particle (Figure 3b) shows that the Ag$_{29}$ NC moieties were attached to the silica shell encapsulating individual AuNRs such that the size and shape of the resulting nanocomposite were guided by that of the AuNR and the thickness of the silica shell. This indicates that by choosing the right morphology of the template nanoparticle, we can obtain plasmonic luminescent nanocomposites of desired size and shape that may act as building blocks for advanced hierarchical metamaterials. A 3D image of a single AuNR@mSiO$_2$@Ag$_{29}$ is presented in Figure 3c (Video S2 contains the corresponding tilt series), where the red color denotes high electron density. For a better understanding of the core−shell structure, some of the atoms were deliberately removed during reconstruction. The underlying AuNR and Ag$_{29}$ NCs on the surface appear in red, making the visualization easier. Since Ag NCs are photosensitive, the PL intensity of the nanocomposite decreased with time as that of the parent Ag$_{29}$ decreased (Figure S3a−c). Figure 4a shows the emission maxima of AuNR@mSiO$_2$@Ag$_{29}$ and that of parent Ag$_{29}$ as a function of time. The results suggest that AuNR@mSiO$_2$@Ag$_{29}$ showed enhanced PL at any point of time as compared to Ag$_{29}$ until their PL was quenched after 2 days. The TEM image of the composite after 48 h (Figure S3d) reveals that the NCs aggregated to form Ag NPs, which explains the quenching of their luminescence. Noble metal NCs show weak PL quantum yield in an aqueous solution mostly due to nonradiative relaxation through surface−ligand motion.[54] However, using poor solvent or electrostatic attraction, they can be aggregated, which leads to significant enhancement of their PL QY.[55,56] Fluorescent NCs and QDs often suffer from aggregation-

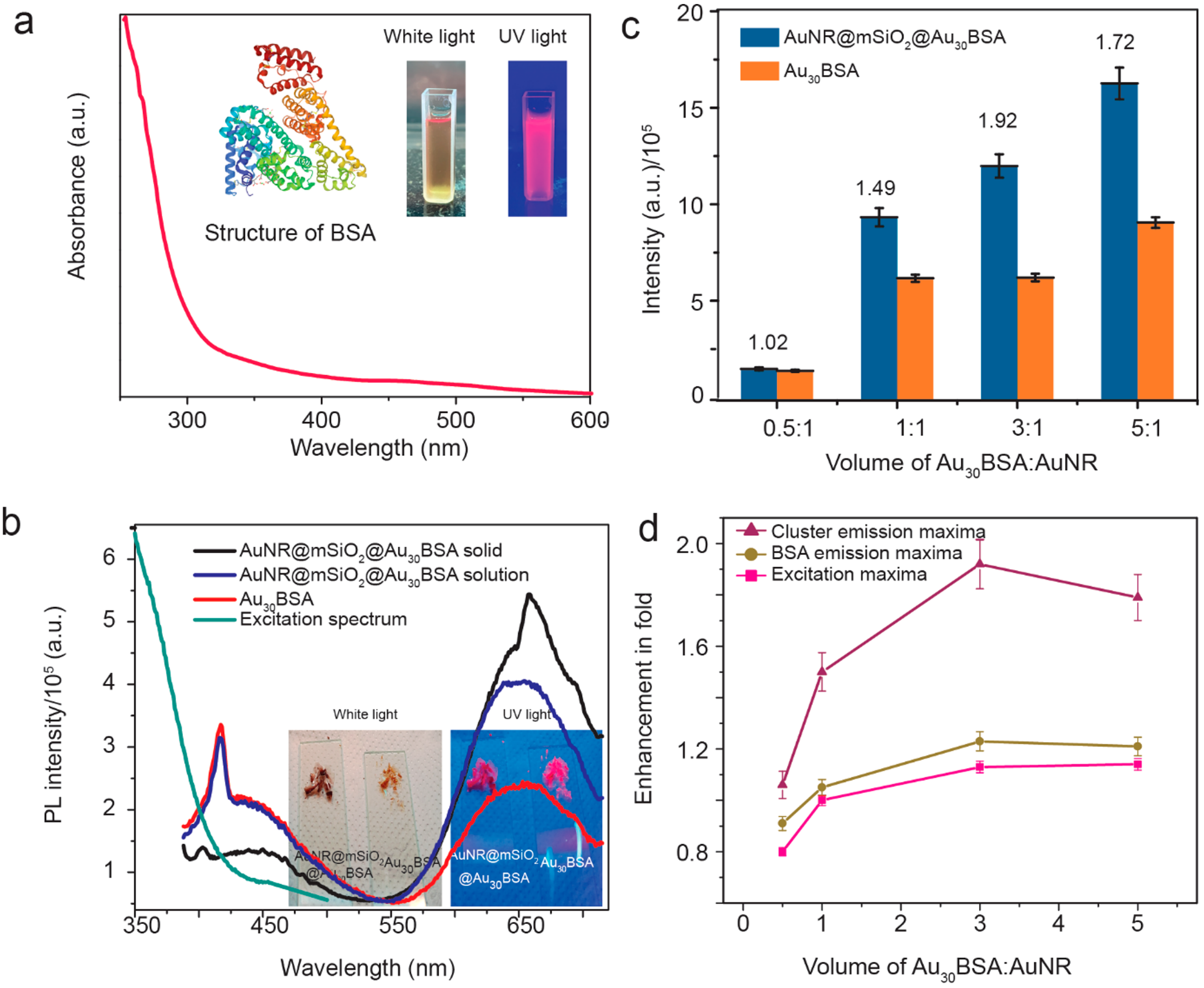

Figure 5. (a) UV−vis absorption spectrum of $Au_{30}BSA$ with the crystal structure of BSA and photographs of $Au_{30}BSA$ NC under white light and UV light (inset). (b) PL emission spectra of $AuNR@mSiO_2@Au_{30}BSA$ in both solution and in solid phases, and blank $Au_{30}BSA$ along, with the excitation spectrum; inset shows photographs of luminescent solid $AuNR@mSiO_2@Au_{30}BSA$ and solid $Au_{30}BSA$. (c) Ratio of PL enhancement compared to free $Au_{30}BSA$ at gradually higher $Au_{30}BSA$ to AuNR concentration ratio. (d) Change in the excitation, protein emission, and cluster emission maximum with increasing $Au_{30}BSA$ concentration.

induced photon reabsorption, nonradiative resonant energy transfer, and/or direct $\pi-\pi$ interactions, and so on, leading to fluorescence quenching during solidification.[57−59] Therefore, efforts are being made to achieve luminescent NCs in the solid state with improved PL properties, which would lead to potential applications in making ecofriendly alternatives for conventional toxic nanophosphores.[60] Here, APTES was added to the aqueous dispersion of $AuNR@mSiO_2@Ag_{29}$ in order to screen electrostatic repulsion between surface NCs, allowing them to aggregate. This aggregated $AuNR@mSiO_2@Ag_{29}$ was precipitated upon centrifugation. As shown in Figure 4b, the pellet thus obtained showed red luminescence under UV light, leaving the supernatant nonluminescent. This pellet was dried under ambient condition in dark to obtain solid $AuNR@mSiO_2@Ag_{29}$. The parent Ag_{29} NC was also solidified following a similar procedure.

Figure 4c shows photographs of solid Ag_{29} and solid $AuNR@mSiO_2@Ag_{29}$ made from the same amount of NC under UV light, where the latter shows bright red luminescence. The PL of solid Ag_{29} was almost completely quenched. The PL spectra of solid $AuNR@mSiO_2@Ag_{29}$ and aqueous $AuNR@mSiO_2@Ag_{29}$ are presented in Figure 4d. In the solid phase, the nanocomposite showed significantly enhanced luminescence along with a dramatic red shift in its emission maximum. Such increase in Stokes shift in the solid state is commonly known due to the greater intermolecular interaction in solid state as compared to in solution. Thus, the resulting nanocomposite has potential in diverse fields as a more efficient fluorophore compared to its constituent NC.

Generalization of the Strategy. A large number of luminescent Au NCs reported in the past decade exhibit unique physicochemical properties depending on the composition of their metallic core and surface ligands. Among these, protein-protected Au NCs are studied extensively for live-cell imaging and diagnostics as well as chemical[61] and biosensing[62] due to their biocompatibility, exceptional stability, and water solubility. We synthesized BSA-protected Au NC, namely, $Au_{30}BSA$, following a reported procedure.[63] Figure 5a shows the characteristic UV−vis absorption spectrum and inset includes photographs of the NC under visible and UV light, showing bright red luminescence. Following the procedure described in the case of Ag_{29}, Au_{30}BSA was anchored to AuNR@mSiO_2−NH_2 to synthesize a AuNR@mSiO_2@Au_{30}BSA nanocomposite. In the case of protein-protected NCs, the tiny metallic cores are almost fully buried within the bulky protein structures, making them difficult to visualize under TEM. However, the attachment of Au_{30}BSA to the silica shell of AuNR@mSiO_2 can be inferred from TEM images of AuNR@mSiO_2@Au_{30}BSA (Figure S4a). Similar to parent Au_{30}BSA, upon excitation at 365 nm, the resulting nanocomposite also showed two maxima in its emission spectrum, one at ∼425 nm due to BSA and another at ∼650 nm due to the core of the NC (Figure 5b). In this case, the PL of the NC was also enhanced in its composite form, as shown in Figure 5b. Owing to the photostability of Au_{30}BSA, AuNR@mSiO_2@Au_{30}BSA showed intense luminescence for more than a month suggesting high colloidal stability of the nanocomposite. Both the blank NC and the composite also showed bright red PL in their solid form (inset of Figure 5b). In this case, the emission maximum of the solid nanocomposite was red-shifted compared to the aqueous dispersion. Maximum loading of Au_{30}BSA to the individual AuNR@mSiO_2 structures was ensured by adding gradually higher amount of Au_{30}BSA to a fixed amount of AuNR@mSiO_2 and comparing their PL spectra with the same concentration of Au_{30}BSA as blank in each case. As shown in Figure 5c, the highest PL enhancement factor of 1.92 was obtained when the AuNR/Au_{30}BSA volume ratio was 1:3. In order to prove that this enhancement was due to plasmonic coupling and not the confinement effect of silica,[64] we measured the enhancement of the excitation and emission spectra of the composite with gradually higher NC concentration and plotted the excitation maximum and the two emission maxima (at ∼420 nm due to the BSA protein and ∼650 nm due to the Au_{30} core) in Figure 5d. With increasing Au_{30}BSA concentration, the change in protein emission maxima followed the trend of the excitation maxima, which is a direct consequence of the change in NC concentration, but the change in emission maximum around 650 nm was much more profound. Since AuNRs primarily scatter at this silica shell thickness, presumably the Purcell effect predominates over FRET.[65] Hence, emission due to the Au_{30} core that overlaps with the LSPR band of AuNRs gets enhanced, but the protein emission is not enhanced. Hence, this observation confirms that the greater PL intensity of the composite than the parent NC is due to plasmon-induced enhancement. Thus, both the luminescent NCs of very different compositions form brighter plasmonic luminescent nanocomposites encapsulating individual AuNRs, using this approach.

■ CONCLUSIONS

In conclusion, we assembled fluorescent Ag_{29} NCs on a versatile anisotropic plasmonic nanoprobe, namely, AuNR, through a mesoporous silica shell. The resulting nanocomposite is structurally precise and well-dispersed in aqueous medium, and it shows enhanced PL in both dispersed and solid phases. The size and shape of the composite are guided by the encapsulated AuNR and therefore are tunable, depending on the AuNR chosen. Using Au_{30}BSA NC, we showed that the proposed approach is not only straightforward but also generic for water-soluble luminescent NCs, irrespective of their composition. Thus, by taking the right pair of NCs and NPs as starting materials for the proposed strategy, one can obtain an attractive nanoprobe for dual-mode bioimaging, targeted drug delivery, therapeutics, or any PL-based sensing application. Structural investigations of such plasmonic luminescent nanocomposites in great detail show their potential to act as luminescent building blocks of defined geometry for engineering advanced nanomaterials.

■ ASSOCIATED CONTENT

Supporting Information

The Supporting Information is available free of charge at https://pubs.acs.org/doi/10.1021/acs.jpcb.1c10207.

Confirmation of silica growth on AuNRs, TEM image of AuNR@Ag_{29}, change in AuNR@mSiO_2@Ag_{29} with time, TEM image of AuNR@mSiO_2@Au_{30}BSA, and its PL excitation and emission at various Au_{30}BSA concentration (PDF)

Tomographic reconstruction of AuNR@mSiO_2 (AVI)

Tomographic reconstruction of AuNR@mSiO_2@Ag_{29} (AVI)

■ AUTHOR INFORMATION

Corresponding Author

Thalappil Pradeep − *DST Unit of Nanoscience and Thematic Unit of Excellence, Department of Chemistry, Indian Institute of Technology Madras, Chennai 600036, India;* orcid.org/0000-0003-3174-534X; Email: pradeep@iitm.ac.in

Authors

Amrita Chakraborty − *DST Unit of Nanoscience and Thematic Unit of Excellence, Department of Chemistry, Indian Institute of Technology Madras, Chennai 600036, India*

Harsh Dave − *DST Unit of Nanoscience and Thematic Unit of Excellence, Department of Chemistry, Indian Institute of Technology Madras, Chennai 600036, India;* Present Address: Department of Bioengineering, University of Texas at Dallas, Richardson, Texas 75080, USA

Biswajit Mondal − *DST Unit of Nanoscience and Thematic Unit of Excellence, Department of Chemistry, Indian Institute of Technology Madras, Chennai 600036, India*

Nonappa − *Faculty of Engineering and Natural Sciences, Tampere University, FI-33720 Tampere, Finland;* orcid.org/0000-0002-6804-4128

Esma Khatun − *DST Unit of Nanoscience and Thematic Unit of Excellence, Department of Chemistry, Indian Institute of Technology Madras, Chennai 600036, India*

Complete contact information is available at: https://pubs.acs.org/10.1021/acs.jpcb.1c10207

Author Contributions

A.C. designed the experiments and carried out samples' preparation. H.D. carried out UV−vis spectroscopy and PL studies. B.M. collected TEM images. N. carried out imaging and electron tomography reconstruction measurements. E.K. synthesized Ag_{29} and Au_{30}BSA NC. The manuscript was written through contributions of all authors.

Notes

The authors declare no competing financial interest.

■ ACKNOWLEDGMENTS

We thank the Department of Science and Technology, Government of India for supporting our research. A.C. thanks the Council of Scientific and Industrial Research and B.M. and E.K thank IIT Madras for their research fellowships. T.P. acknowledges funding for the Centre of Excellence on Molecular Materials and Functions under the Institution of Eminence scheme of IIT Madras. We acknowledge the support from the Ministry of Education and Culture (FICORE-2021 through MEC Global pilot program) and the Photonics Research and Innovation (PREIN) flagship and facilities at the OtaNano-Nanomicroscopy Center (Aalto-NMC).

■ REFERENCES

(1) Simeonidis, K.; Martinez-Boubeta, C.; Zamora-Pérez, P.; Rivera-Gil, P.; Kaprara, E.; Kokkinos, E.; Mitrakas, M. Implementing nanoparticles for competitive drinking water purification. *Environ. Chem. Lett.* **2019**, *17*, 705−719.

(2) Rani, A.; Reddy, R.; Sharma, U.; Mukherjee, P.; Mishra, P.; Kuila, A.; Sim, L. C.; Saravanan, P. A review on the progress of nanostructure materials for energy harnessing and environmental remediation. *J. Nanostructure Chem.* **2018**, *8*, 255−291.

(3) Tyo, E. C.; Vajda, S. Catalysis by clusters with precise numbers of atoms. *Nat. Nanotechnol.* **2015**, *10*, 577−588.

(4) Wang, Y.; Zhou, X.; Xu, C.; Jin, Y.; Li, B. Gold Nanorods as Visual Sensing Platform for Chiral Recognition with Naked Eyes. *Sci. Rep.* **2018**, *8*, 5296.

(5) Wolfbeis, O. S. An overview of nanoparticles commonly used in fluorescent bioimaging. *Chem. Soc. Rev.* **2015**, *44*, 4743−4768.

(6) Chakraborty, I.; Pradeep, T. Atomically Precise Clusters of Noble Metals: Emerging Link between Atoms and Nanoparticles. *Chem. Rev.* **2017**, *117*, 8208−8271.

(7) Tan, X.; Jin, R. Ultrasmall metal nanoclusters for bio-related applications. *WIREs Nanomedic. Nanobiotechnol.* **2013**, *5*, 569−581.

(8) Eggeling, C.; Widengren, J.; Rigler, R.; Seidel, C. A. M. Photobleaching of Fluorescent Dyes under Conditions Used for Single-Molecule Detection: Evidence of Two-Step Photolysis. *Anal. Chem.* **1998**, *70*, 2651−2659.

(9) Kairdolf, B. A.; Smith, A. M.; Stokes, T. H.; Wang, M. D.; Young, A. N.; Nie, S. Semiconductor Quantum Dots for Bioimaging and Biodiagnostic Applications. *Annu. Rev. of Anal. Chem.* **2013**, *6*, 143−162.

(10) Montalti, M.; Cantelli, A.; Battistelli, G. Nanodiamonds and silicon quantum dots: ultrastable and biocompatible luminescent nanoprobes for long-term bioimaging. *Chem. Soc. Rev.* **2015**, *44*, 4853−4921.

(11) Wang, Y.; Hu, A. Carbon quantum dots: synthesis, properties and applications. *J. Mater. Chem. C* **2014**, *2*, 6921−6939.

(12) Weng, J.; Ren, J. Luminescent Quantum Dots: A Very Attractive and Promising Tool in Biomedicine. *Curr. Med. Chem.* **2006**, *13*, 897−909.

(13) Retnakumari, A.; Setua, S.; Menon, D.; Ravindran, P.; Muhammed, H.; Pradeep, T.; Nair, S.; Koyakutty, M. Molecular-receptor-specific, non-toxic, near-infrared-emitting Au cluster-protein nanoconjugates for targeted cancer imaging. *Nanotechnology* **2010**, *21*, 055103.

(14) Nonappa. Luminescent gold nanoclusters for bioimaging applications. *Beilstein J. Nanotechnol.* **2020**, *11*, 533−546.

(15) Hynninen, V.; Chandra, S.; Das, S.; Amini, M.; Dai, Y.; Lepikko, S.; Mohammadi, P.; Hietala, S.; Ras, R. H. A.; Sun, Z.; et al. Luminescent Gold Nanocluster-Methylcellulose Composite Optical Fibers with Low Attenuation Coefficient and High Photostability. *Small* **2021**, *17*, 2005205.

(16) Chandra, S.; Nonappa; Beaune, G.; Som, A.; Zhou, S.; Lahtinen, J.; Jiang, H.; Timonen, J. V. I.; Ikkala, O.; Ras, R. H. A. Highly Luminescent Gold Nanocluster Frameworks. *Adv. Opt. Mater.* **2019**, *7*, 1900620.

(17) Yu, H.; Peng, Y.; Yang, Y.; Li, Z.-Y. Plasmon-enhanced light−matter interactions and applications. *npj Comput. Mater.* **2019**, *5*, 45.

(18) Xia, H.-X.; Yang, X.-Q.; Song, J.-T.; Chen, J.; Zhang, M.-Z.; Yan, D.-M.; Zhang, L.; Qin, M.-Y.; Bai, L.-Y.; Zhao, Y.-D.; et al. Folic acid-conjugated silica-coated gold nanorods and quantum dots for dual-modality CT and fluorescence imaging and photothermal therapy. *J. Mater. Chem. B* **2014**, *2*, 1945−1953.

(19) Alkilany, A. M.; Thompson, L. B.; Boulos, S. P.; Sisco, P. N.; Murphy, C. J. Gold nanorods: their potential for photothermal therapeutics and drug delivery, tempered by the complexity of their biological interactions. *Adv. Drug Delivery Rev.* **2012**, *64*, 190−9.

(20) Drisko, G. L.; Sanchez, C. Hybridization in Materials Science − Evolution, Current State, and Future Aspirations. *Eur. J. Inorg. Chem.* **2012**, *2012*, 5097−5105.

(21) Sanchez, C.; Belleville, P.; Popall, M.; Nicole, L. Applications of advanced hybrid organic−inorganic nanomaterials: from laboratory to market. *Chem. Soc. Rev.* **2011**, *40*, 696−753.

(22) Sailor, M. J.; Park, J. H. Hybrid nanoparticles for detection and treatment of cancer. *Adv. Mater. (Deerfield Beach, Fla.)* **2012**, *24*, 3779−802.

(23) Melancon, M. P.; Zhou, M.; Li, C. Cancer Theranostics with Near-Infrared Light-Activatable Multimodal Nanoparticles. *Acc. Chem. Res.* **2011**, *44*, 947−956.

(24) Luo, T.; Huang, P.; Gao, G.; Shen, G.; Fu, S.; Cui, D.; Zhou, C.; Ren, Q. Mesoporous silica-coated gold nanorods with embedded indocyanine green for dual mode X-ray CT and NIR fluorescence imaging. *Opt. Express* **2011**, *19*, 17030−9.

(25) Sun, H.; Yuan, Q.; Zhang, B.; Ai, K.; Zhang, P.; Lu, L. GdIII functionalized gold nanorods for multimodal imaging applications. *Nanoscale* **2011**, *3*, 1990−1996.

(26) Lee, S.; Sim, K.; Moon, S. Y.; Choi, J.; Jeon, Y.; Nam, J.-M.; Park, S.-J. Controlled Assembly of Plasmonic Nanoparticles: From Static to Dynamic Nanostructures. *Adv. Mater.* **2021**, *33*, 2007668.

(27) Nonappa; Lahtinen, T.; Haataja, J. S.; Tero, T.-R.; Häkkinen, H.; Ikkala, O. Template-Free Supracolloidal Self-Assembly of Atomically Precise Gold Nanoclusters: From 2D Colloidal Crystals to Spherical Capsids. *Angew. Chem., Int. Ed.* **2016**, *55*, 16035−16038.

(28) Chakraborty, A.; Fernandez, A. C.; Som, A.; Mondal, B.; Natarajan, G.; Paramasivam, G.; Lahtinen, T.; Häkkinen, H.; Nonappa; Pradeep, T. Atomically Precise Nanocluster Assemblies Encapsulating Plasmonic Gold Nanorods. *Angew. Chem., Int. Ed.* **2018**, *57*, 6522−6526.

(29) Som, A.; Chakraborty, I.; Maark, T. A.; Bhat, S.; Pradeep, T. Cluster-Mediated Crossed Bilayer Precision Assemblies of 1D Nanowires. *Adv. Mater.* **2016**, *28*, 2827−2833.

(30) Samal, A. K.; Sreeprasad, T. S.; Pradeep, T. Investigation of the role of $NaBH_4$ in the chemical synthesis of gold nanorods. *J. Nanopart. Res.* **2010**, *12*, 1777−1786.

(31) Gorelikov, I.; Matsuura, N. Single-Step Coating of Mesoporous Silica on Cetyltrimethyl Ammonium Bromide-Capped Nanoparticles. *Nano Lett.* **2008**, *8*, 369−373.

(32) Liu, J.; Detrembleur, C.; De Pauw-Gillet, M.-C.; Mornet, S.; Jérôme, C.; Duguet, E. Gold Nanorods Coated with Mesoporous Silica Shell as Drug Delivery System for Remote Near Infrared Light-Activated Release and Potential Phototherapy. *Small* **2015**, *11*, 2323−2332.

(33) van der Linden, M.; Barendregt, A.; van Bunningen, A.; Chin, P.; Thies-Weesie, D.; De Groot, F.; Meijerink, A. Characterisation, degradation and regeneration of luminescent Ag_{29} clusters in solution. *Nanoscale* **2016**, *8*, 19901−19909.

(34) Mohanty, J. S.; Baksi, A.; Lee, H.; Pradeep, T. Noble metal clusters protected with mixed proteins exhibit intense photoluminescence. *RSC Adv.* **2015**, *5*, 48039−48045.

(35) Mastronarde, D. N. SerialEM: A Program for Automated Tilt Series Acquisition on Tecnai Microscopes Using Prediction of Specimen Position. *Microsc. Microanal.* **2003**, *9*, 1182−1183.

(36) Mastronarde, D. N. Automated electron microscope tomography using robust prediction of specimen movements. *J. Struct. Biol.* **2005**, *152*, 36−51.

(37) Nonappa; Engelhardt, P. Electron Tomography of Whole Mounts. *Wiley Anal. Sci.* **2019**, *21*, 22−24.

(38) Kremer, J. R.; Mastronarde, D. N.; McIntosh, J. R. Computer Visualization of Three-Dimensional Image Data Using IMOD. *J. Struct. Biol.* **1996**, *116*, 71−76.

(39) Dulkeith, E.; Morteani, A. C.; Niedereichholz, T.; Klar, T. A.; Feldmann, J.; Levi, S. A.; van Veggel, F. C.; Reinhoudt, D. N.; Möller, M.; Gittins, D. I. Fluorescence quenching of dye molecules near gold nanoparticles: radiative and nonradiative effects. *Phys. Rev. Lett.* **2002**, *89*, 203002.

(40) Li, S.; Zhang, T.; Zhu, Z.; Gao, N.; Xu, Q.-H. Lighting up the gold nanoparticles quenched fluorescence by silver nanoparticles: a separation distance study. *RSC Adv.* **2016**, *6*, 58566−58572.

(41) Reineck, P.; Gómez, D.; Ng, S. H.; Karg, M.; Bell, T.; Mulvaney, P.; Bach, U. Distance and Wavelength Dependent Quenching of Molecular Fluorescence by Au@SiO_2 Core−Shell Nanoparticles. *ACS Nano* **2013**, *7*, 6636−6648.

(42) Marques, M. E.; Mansur, A. A. P.; Mansur, H. S. Chemical functionalization of surfaces for building three-dimensional engineered biosensors. *Appl. Surf. Sci.* **2013**, *275*, 347−360.

(43) Villa, S.; Riani, P.; Locardi, F.; Canepa, F. Functionalization of Fe_3O_4 NPs by Silanization: Use of Amine (APTES) and Thiol (MPTMS) Silanes and Their Physical Characterization. *Materials (Basel)* **2016**, *9*, 826.

(44) Shang, L.; Yang, L.; Stockmar, F.; Popescu, R.; Trouillet, V.; Bruns, M.; Gerthsen, D.; Nienhaus, G. U. Microwave-assisted rapid synthesis of luminescent gold nanoclusters for sensing Hg2+ in living cells using fluorescence imaging. *Nanoscale* **2012**, *4*, 4155−4160.

(45) Adhikari, B.; Banerjee, A. Facile Synthesis of Water-Soluble Fluorescent Silver Nanoclusters and HgII Sensing. *Chem. Mater.* **2010**, *22*, 4364−4371.

(46) Shang, L.; Azadfar, N.; Stockmar, F.; Send, W.; Trouillet, V.; Bruns, M.; Gerthsen, D.; Nienhaus, G. U. One-Pot Synthesis of Near-Infrared Fluorescent Gold Clusters for Cellular Fluorescence Lifetime Imaging. *Small* **2011**, *7*, 2614−2620.

(47) Jiang, R.; Li, B.; Fang, C.; Wang, J. Metal/Semiconductor Hybrid Nanostructures for Plasmon-Enhanced Applications. *Adv. Mater.* **2014**, *26*, 5274−5309.

(48) Li, J.-F.; Li, C.-Y.; Aroca, R. F. Plasmon-enhanced fluorescence spectroscopy. *Chem. Soc. Rev.* **2017**, *46*, 3962−3979.

(49) Goris, B.; Bals, S.; Van den Broek, W.; Carbó-Argibay, E.; Gómez-Graña, S.; Liz-Marzán, L. M.; Van Tendeloo, G. Atomic-scale determination of surface facets in gold nanorods. *Nat. Mater.* **2012**, *11*, 930−935.

(50) Xiang, Y.; Wu, X.; Liu, D.; Jiang, X.; Chu, W.; Li, Z.; Ma, Y.; Zhou, W.; Xie, S. Formation of Rectangularly Shaped Pd/Au Bimetallic Nanorods: Evidence for Competing Growth of the Pd Shell between the {110} and {100} Side Facets of Au Nanorods. *Nano Lett.* **2006**, *6*, 2290−2294.

(51) Cho, E. C.; Camargo, P. H. C.; Xia, Y. Synthesis and Characterization of Noble-Metal Nanostructures Containing Gold Nanorods in the Center. *Adv. Mater.* **2010**, *22*, 744−748.

(52) Carbó-Argibay, E.; Rodríguez-González, B. Controlled Growth of Colloidal Gold Nanoparticles: Single-Crystalline versus Multiply-twinned Particles. *Isr. J. Chem.* **2016**, *56*, 214−226.

(53) Zhu, J.; Chang, H.; Li, J. J.; Li, X.; Zhao, J. W. Using silicon-coated gold nanoparticles to enhance the fluorescence of CdTe quantum dot and improve the sensing ability of mercury (II). *Spectrochim. Acta A Mol. Biomol. Spectrosc.* **2018**, *188*, 170−178.

(54) Wu, Z.; Jin, R. On the Ligand's Role in the Fluorescence of Gold Nanoclusters. *Nano Lett.* **2010**, *10*, 2568−2573.

(55) Goswami, N.; Yao, Q.; Luo, Z.; Li, J.; Chen, T.; Xie, J. Luminescent Metal Nanoclusters with Aggregation-Induced Emission. *J. Phys. Chem. Lett.* **2016**, *7*, 962−975.

(56) Goswami, N.; Lin, F.; Liu, Y.; Leong, D. T.; Xie, J. Highly Luminescent Thiolated Gold Nanoclusters Impregnated in Nanogel. *Chem. Mater.* **2016**, *28*, 4009−4016.

(57) Chen, Y.; Zheng, M.; Xiao, Y.; Dong, H.; Zhang, H.; Zhuang, J.; Hu, H.; Lei, B.; Liu, Y. A Self-Quenching-Resistant Carbon-Dot Powder with Tunable Solid-State Fluorescence and Construction of Dual-Fluorescence Morphologies for White Light-Emission. *Adv. Mater. (Deerfield Beach, Fla.)* **2016**, *28*, 312−318.

(58) Gan, Z.; Di, Y.; Huang, S.; Shen, J.; Yang, L.; Zhang, X. Modulating the fluorescent color of carbon nanodots via photon reabsorption and carbonization degree. *Appl. Phys. Lett.* **2017**, *111*, 241903.

(59) Gan, Z.; Xu, H.; Fu, Y. Photon Reabsorption and Nonradiative Energy-Transfer-Induced Quenching of Blue Photoluminescence from Aggregated Graphene Quantum Dots. *J. Phys. Chem. C* **2016**, *120*, 29432−29438.

(60) Huang, H.-Y.; Cai, K.-B.; Talite, M. J.; Chou, W.-C.; Chen, P.-W.; Yuan, C.-T. Coordination-induced emission enhancement in gold-nanoclusters with solid-state quantum yields up to 40% for eco-friendly, low-reabsorption nano-phosphors. *Sci. Rep.* **2019**, *9*, 4053.

(61) Senthamizhan, A.; Celebioglu, A.; Uyar, T. Real-time selective visual monitoring of Hg2+ detection at ppt level: An approach to lighting electrospun nanofibers using gold nanoclusters. *Sci. Rep.* **2015**, *5*, 10403.

(62) Chen, Z.; Qian, S.; Chen, X.; Gao, W.; Lin, Y. Protein-templated gold nanoclusters as fluorescence probes for the detection of methotrexate. *Analyst* **2012**, *137*, 4356−4361.

(63) Chevrier, D. M.; Thanthirige, V. D.; Luo, Z.; Driscoll, S.; Cho, P.; MacDonald, M. A.; Yao, Q.; Guda, R.; Xie, J.; Johnson, E. R.; Chatt, A.; et al. Structure and formation of highly luminescent protein-stabilized gold clusters. *Chem. Sci.* **2018**, *9*, 2782−2790.

(64) Zhou, R.; Sun, S.; Li, C.; Wu, L.; Hou, X.; Wu, P. Enriching Mn-Doped ZnSe Quantum Dots onto Mesoporous Silica Nanoparticles for Enhanced Fluorescence/Magnetic Resonance Imaging Dual-Modal Bio-Imaging. *ACS Appl. Mater. Interfaces* **2018**, *10*, 34060−34067.

(65) Li, M.; Cushing, S. K.; Wu, N. Plasmon-enhanced optical sensors: a review. *Analyst* **2015**, *140*, 386−406.